

AD-A248 344



REPORT DOCUMENTATION PAGE

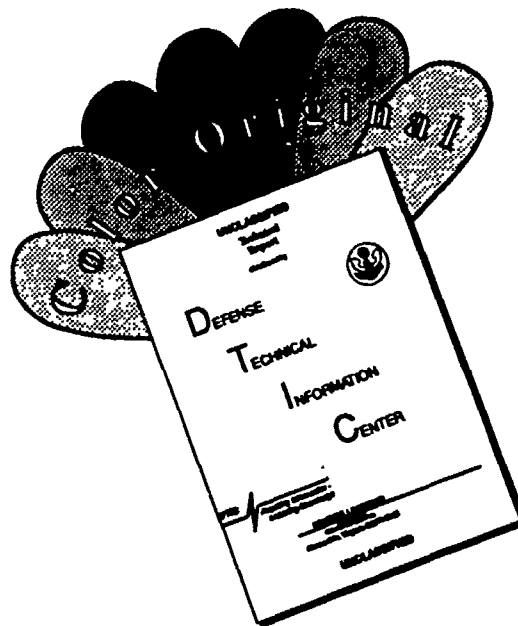
Unclassified			1b. RESTRICTIVE MARKINGS	
2a. SECURITY CLASSIFICATION AUTHORITY			3. DISTRIBUTION/AVAILABILITY OF REPORT	
2b. DECLASSIFICATION/DOWNGRADING SCHEDULE APR 08 1992			Distribution Unlimited. Approved for Public Release	
4. PERFORMING ORGANIZATION REPORT NUMBER			5. MONITORING ORGANIZATION REPORT NUMBER(S) AFOSR-TR- 92 0192	
6a. NAME OF PERFORMING ORGANIZATION Tufts University		6b. OFFICE SYMBOL (If applicable)	7a. NAME OF MONITORING ORGANIZATION AFOSR/NL	
6c. ADDRESS (City, State, and ZIP Code) Dept. of Physics and Astronomy Tufts University Medford, MA02155		7b. ADDRESS (City, State, and ZIP Code) Bolling Air Force Base Washington, DC 20332		
8a. NAME OF FUNDING/SPONSORING ORGANIZATION AFOSR/NL		8b. OFFICE SYMBOL (If applicable) NL	9. PROCUREMENT INSTRUMENT IDENTIFICATION NUMBER Grant AFOSR-89-0147	
8c. ADDRESS (City, State, and ZIP Code) Bolling Air Force Base Washington, DC 20332		10. SOURCE OF FUNDING NUMBERS		
		PROGRAM ELEMENT NO. 61102F	PROJECT NO. 2311	TASK NO. A1
		WORK UNIT ACCESSION NO. NA		
11. TITLE (Include Security Classification) COMSTOC IV: Multiwaveband Observations of Sunspot and Plage-Associated Coronal Emission				
12. PERSONAL AUTHOR(S) Jeffrey W. Brosius, Robert F. Willson, Gordon D. Holman, and Joan T. Schmelz				
13a. TYPE OF REPORT Interim Reprint		13b. TIME COVERED FROM TO		15. PAGE COUNT 34
14. DATE OF REPORT (Year, Month, Day) January 22, 1992				
16. SUPPLEMENTARY NOTATION Paper published in the Astrophysical Journal (February 1992)				
17. COSATI CODES			18. SUBJECT TERMS (Continue on reverse if necessary and identify by block number)	
FIELD	GROUP	SUB-GROUP		
			Sun: Xorona; Sun - radio radiation; Sun - X-rays	
19. ABSTRACT (Continue on reverse if necessary and identify by block number) Simultaneous observations of an active region located near central meridian were obtained with the Very Large Array, the Solar Maximum Mission X-ray Polychromator, and the Beijing Observatory magnetograph on 18 December 1987, during the Coronal Magnetic Structures Observing Campaign (COMSTOC). An asymmetric loop-like structure connects the strong leading sunspot with a nearby region of opposite polarity. Both 6 and 20 cm emission lies along this structure, rather than over the sunspot, with higher frequency emission originating closer to the footpoint inside the sunspot. The 20 cm emission is due to a superposition of 2nd and 3rd harmonic gyroemission, where the field strength is 16- G- 300 G, while the 6 cm emission is due to the 3rd harmonic gyroemission from a region where the magnetic field strength ranges from 547 - 583 G. A high value of the Alfven speed of 40,000 km/sec, is obtained at the location of the 6 cm source, with somewhat lower values of 10,000 - 20,000 km/sec, at the location of the 20 cm emission. At the location of the 6 cm source, the plasma temperature diminishes with height from				
20. DISTRIBUTION/AVAILABILITY OF ABSTRACT <input checked="" type="checkbox"/> UNCLASSIFIED/UNLIMITED <input type="checkbox"/> SAME AS RPT <input type="checkbox"/> DTIC USERS			21. ABSTRACT SECURITY CLASSIFICATION	
22a. NAME OF RESPONSIBLE INDIVIDUAL Dr. Henry R. Radoski			22b. TELEPHONE (Include Area Code) (202) 767-4906	22c. OFFICE SYMBOL

11 8 FEB '92

2.5×10^6 K at 5000 km to 1.3×10^6 K at 15,000 km.

The X-ray data associated with an area of trailing plage were used to predict the brightness temperature structure due to thermal bremsstrahlung emission in the 6 and 20 cm wavebands. The predicted 6 cm brightness temperature in and around the location of the X-ray peak is low, consistent with that observed in the central portions of the plage, but the high 20 cm polarization requires the presence of cool absorbing plasma overlying the hot plasma observed in X-rays. Two different models for interpreting these observations are described.

DISCLAIMER NOTICE



THIS DOCUMENT IS BEST QUALITY AVAILABLE. THE COPY FURNISHED TO DTIC CONTAINED A SIGNIFICANT NUMBER OF COLOR PAGES WHICH DO NOT REPRODUCE LEGIBLY ON BLACK AND WHITE MICROFICHE.

CoMStOC IV: Multiwaveband Observations of Sunspot and Plage-Associated Coronal Emission

Jeffrey W. Brosius
Laboratory for Astronomy and Solar Physics, NASA/GSFC
and
ST Systems Corporation

Robert F. Willson
Tufts University

Gordon D. Holman
Laboratory for Astronomy and Solar Physics, NASA/GSFC

Joan T. Schmelz
Applied Research Corporation and Lockheed

To appear in *The Astrophysical Journal*, February 1992

92-08981



92 4 07 068

18 FEB 1992

Abstract

Simultaneous observations of an active region located near central meridian were obtained with the Very Large Array, the Solar Maximum Mission X-Ray Polychromator, and the Beijing Observatory magnetograph on 18 December 1987, during the Coronal Magnetic Structures Observing Campaign (CoMStOC). An asymmetric loop-like structure connects the strong leading sunspot with a nearby region of opposite polarity. Both 6 and 20 cm emission lie along this structure, rather than over the sunspot, with higher frequency emission originating closer to the footpoint inside the sunspot. The 20 cm emission is due to a superposition of 2nd and 3rd harmonic gyroemission, where the field strength is 160 G - 300 G, while the 6 cm emission is due to 3rd harmonic gyroemission from a region where the magnetic field strength ranges from 547 G - 583 G. A high value of the Alfvén speed, $\sim 40,000$ km/sec, is obtained at the location of the 6 cm source, with somewhat lower values, $\sim 10,000 - 20,000$ km/sec, at the location of the 20 cm emission. At the location of the 6 cm source, the plasma temperature diminishes with height from 2.5×10^6 K at ~ 5000 km to 1.3×10^6 K at $\sim 15,000$ km.

The X-ray data associated with an area of trailing plage were used to predict the brightness temperature structure due to thermal bremsstrahlung emission in the 6 and 20 cm wavebands. The predicted 6 cm brightness temperature in and around the location of the X-ray peak is low, consistent with our lack of observed 6 cm plage emission. The predicted 20 cm brightness temperature is consistent with that observed in the central portions of the plage, but the high 20 cm polarization requires the presence of cool ($T_e \leq 5 \times 10^5$ K), absorbing plasma overlying the hot plasma observed in X-rays. Two different models for interpreting these observations are described.



Accession For	
NTIS GRA&I	<input checked="" type="checkbox"/>
DTIC TAB	<input type="checkbox"/>
Unannounced	<input type="checkbox"/>
Justification	
By _____	
Distribution/	
Availability Codes	
Dist	Avail and/or Special
A-1	

1 Introduction

Observations of coronal loops taken with the Very Large Array (VLA) show that emission at different wavelengths originates at different heights, with longer wavelengths corresponding to higher levels. Synthesis maps at 20 cm wavelength, for example, outline loop-like structures that stretch across regions of opposite magnetic polarity (Lang, Willson, and Rayrole 1982) while observations at shorter wavelengths (2 and 6 cm) generally indicate sources that lie along the legs of loops (Alissandrakis and Kundu 1982; Lang and Willson 1982; Lang, Willson and Gaizauskas 1983; Strong, Alissandrakis and Kundu 1984). The 20 cm loops are similar to their X-ray counterparts, for the loops detected have similar sizes, shapes, and brightness temperatures.

Although the X-ray emission is attributed to thermal bremsstrahlung and atomic line emission from hot ($T_e \sim 3 \times 10^6$ K) coronal plasma, the microwave emission may be due to either thermal bremsstrahlung or to gyroresonance emission from thermal electrons spiralling along coronal magnetic field lines. In order to determine which of these mechanisms is dominant, it is necessary to know the electron temperature and emission measure of the plasma so that the brightness temperature at a particular wavelength can be calculated and compared with the observed values. Observations of soft X-ray spectral lines obtained by the X-ray Polychromator (XRP) aboard the Solar Maximum Mission (SMM) satellite, for example, can yield estimates of the electron temperature, emission measure, and density in quiescent loops. These parameters have been combined with plausible estimates for the magnetic scale height and the harmonic to show that the microwave-emitting plasma can be optically thick to either thermal bremsstrahlung or gyroresonance emission at 20 cm wavelength (Lang, Willson, and Rayrole 1982; McConnell and Kundu 1983; Shevgaonkar and Kundu 1984; Gary and Hurford 1987).

Direct comparison of 6 cm and soft X-ray emission has confirmed the importance of gyroresonance emission at this wavelength. However, the brightest 6 cm sources are usually not associated with the brightest X-ray sources and the detailed correspondence between the radiation at these two wavelengths is poor (Schmahl et al. 1982; Webb et al. 1983). The reason for this is that 6 cm gyroresonance emission typically occurs in the strong magnetic fields above sunspots, while the X-ray emission is usually most intense between regions of opposite magnetic polarity. Thermal bremsstrahlung at 6 cm is often too optically thin to be detected.

More recent comparisons between simultaneous 20 cm and XRP images have shown better agreement between the emission at these wavelengths, although there are significant differences (Webb et al. 1987; Lang et al. 1987a,b; Nitta et al. 1991 - CoMStOC I). The 20 cm maps suggest the presence of both cool and hot plasmas in different regions that are not detected in X-rays, and there is X-ray emitting plasma that remains invisible at 20 cm. Although thermal bremsstrahlung could explain the bulk of the 20 cm emission, the detection of a line-like enhancement in the brightness spectrum at the apex of one coronal loop suggests the dominance of gyroresonance emission in that part of the loop (Willson 1985).

In this paper we describe the results of simultaneous VLA and XRP observations of a solar active region obtained during the Coronal Magnetic Structures Observing Campaign (CoMStOC). The primary objective of CoMStOC was to obtain quantitative information about the plasma and magnetic field structure above solar active regions by comparing the microwave and soft X-ray data with theoretical models (Holman and Kundu 1985; Brosius and Holman 1988, 1989) and

photospheric magnetic field measurements. In Section 2 we present and discuss the coordinated observations: VLA observations at four different frequencies in each of the 6 and 20 cm wavebands, XRP spectral and image data, and a photospheric longitudinal magnetogram from Beijing Observatory. In Section 3 we analyze and interpret the VLA, XRP, and magnetograph data in terms of physical models. In Section 4 we summarize our conclusions and their implications.

2 Observations and Data Analysis

2.1 VLA Observations

The VLA (B configuration) was used to observe the active region AR 4906 (S34.5, E17.7 at 1300 UT) between 1440 UT and 2300 UT on 18 December 1987. The entire array of 27 antennas was used at four frequencies in the 20 cm band (1375, 1420, 1550, and 1665 MHz) and four in the 6 cm band (4600, 4700, 4800, and 4900 MHz) with bandwidths of 12.5 MHz. The half-power beamwidth of the individual antennas ranged between 29' and 34'.7 at 20 cm, with synthesized beamwidths of 4". At 6 cm, the primary beamwidths ranged from 9'.7 to 10'.4, with synthesized beamwidths of 1". One pair of frequencies was observed for about 5 minutes, so that all eight could be observed in about twenty minutes. The data were sampled every 10 s and calibrated using observations of PKS1655+078. Corrections were made for the difference in the signals from high temperature noise diodes located on four of the antennas. The temperatures of these sources were measured across each band prior to the observations. The data were edited and calibrated with the standard solar procedures at the VLA, and used to make synthesis maps of both the total intensity, I , and Stokes parameter, V , during the 8.5 hour interval at all eight frequencies. Examination of the fringe visibility on several baselines indicated no variations that could be attributed to solar bursts or interference.

Figure 1a shows the frequency-averaged 20 cm map with two main components: the source on the right is associated with the sunspot and the one on the left, which is $\sim 50\%$ left-hand circularly polarized, is associated with the plage. Individual maps at the four 20 cm frequencies (Fig. 2) show that there is a systematic difference in the structure of the 20 cm emission at these frequencies. The sharply defined peak of the sunspot source systematically shifts by $\sim 10''$ in the direction of the 6 cm source (Fig. 1b) from 1375 MHz to 1665 MHz. This is a manifestation of gyroresonance as the dominant emission mechanism: as the observing frequency changes, the magnetic field strength required to stimulate gyroresonance emission also changes; the appropriate field strength is at a slightly different location, resulting in a shift of the radio source with observing frequency.

In the B-configuration VLA, the maximum fringe spacing is $\sim 225''$ at 20 cm and $66''$ at 6 cm. No information is available concerning sources larger than these critical limits, so possible extended, low brightness temperature structures will be resolved out (see CoMStOC I for a more detailed discussion). The 6 and 20 cm sources seen in Figure 1a,b are smaller than their respective critical sizes, suggesting that no emission from the sources seen in these maps was resolved out. Furthermore, no significant changes in structure or brightness temperature ($< 15\%$) were found between the maps produced using the standard CLEAN algorithms and those produced using the Maximum Entropy Method (MEM) (Cornwell 1986, Bastian 1987). The MEM algorithm is better able to restore large-scale structure (as long as it is smaller than the maximum fringe spacing)

than is CLEAN. Thus the similarity of the MEM and the CLEAN maps indicates that there is no evidence for unresolved large-scale structure in either the 6 or 20 cm maps. Neither CLEAN nor MEM, of course, is capable of restoring the quiet sun background contribution, which is $\sim 4 \times 10^4$ K at 6 cm and $\sim 1 \times 10^5$ K at 20 cm.

2.2 XRP Observations

The XRP Flat Crystal Spectrometer (Acton et al. 1980), collimated to 14" FWHM, could build images by rastering over a portion of a $4' \times 4'$ area with a minimum pixel spacing of 5", or scan a series of spectral lines at one or more spatial locations. XRP mapped AR 4906 in the Fe XVII resonance line at 15.01 Å, the most sensitive line at active region temperatures. This map (Fig. 1c) shows two peaks of emission: the weaker source on the right lies between the sunspot and a nearby region of opposite polarity; the stronger source on the left is associated with the trailing area of plage (see Fig. 1d).

A spectroscopic scan (between 13 and 19 Å) was done at the brightest Fe XVII pixel (marked with an "X" in Fig. 1) in the SMM orbit beginning at 0343 UT on 1987 December 18. Analysis of these spectral data follows the procedure outlined in CoMStOC I. The emissivity calculations from Mewe, Gronenschild, and van den Oord (1985) and the coronal abundances of Meyer (1985) were used to calculate the electron temperatures from five selected line flux ratios. Each of these ratios varies by a factor of 10 or more in the temperature range of interest ($2-4 \times 10^6$ K); this steep gradient makes the ratio sensitive to small changes in temperature and relatively insensitive to systematic uncertainties such as relative flux calibrations, elemental abundance variations, or errors in the atomic parameters. (See CoMStOC I for a detailed discussion of these calculations and possible sources of error.) These values and their uncertainties (statistical only) are listed in Table 1. The uncertainties in the weighted mean include systematic as well as statistical uncertainties. The column emission measure corresponding to each temperature in Table 1 was computed using the O VIII line flux, which has an emissivity curve with a broad, flat response in the range of interest; therefore, the emission measure determined using this line is relatively insensitive to possible errors in temperature. Once again, the uncertainties on the individual entries are statistical only (dominated by the uncertainty in the O VIII line flux) while the weighted mean includes systematic as well as statistical uncertainties.

XRP mapped AR 4906 at the peaks of five bright resonance lines—O VIII, Ne IX, Fe XVII, Mg XI, and Fe XVIII—in the SMM orbit beginning at 1134 UT on 1987 December 18. Ratios of these images can be used to determine the spatial structure of the plasma parameters across the region (as was done in CoMStOC I). Unfortunately, AR 4906 was relatively weak and, although Fe XVII was observed throughout the region, significant counts were observed in only one other line, O VIII, near the brightest central areas of the plage. The O VIII/Fe XVII flux ratio varies by only a factor of about five in the temperature range $2-4 \times 10^6$ K, making it more sensitive to errors in flux calibration, elemental abundance, and atomic parameters than the line ratios available at the brightest Fe XVII pixel. Even though the data were taken 8 hours apart, the resulting electron temperatures and emission measures obtained with the O VIII/Fe XVII flux ratio from the spectroscopic and image data were equal at the same location. This indicates that the active region was stable during the observation period. Also, GOES soft X-ray data show no significant activity at or between the times of these observations.

A comparison of electron temperatures obtained from various line flux ratios at the location of the spectroscopic scan leads to the conclusion that the Fe XVII emissivity is inconsistent with that of the other lines by a factor of ~ 2.75 . For greater detail see CoMStOC I, where the factor was found to be lower (~ 2.25), but the difference is within the uncertainty of the measurements. This emissivity "correction factor" is used to obtain temperature and emission measure maps (Figures 1e and 1f) from the O VIII/Fe XVII map flux ratios. Maps of the predicted microwave brightness temperatures at 20 cm and 6 cm are also shown (Figures 1g and 1h) and discussed further in Section 3.3. These maps were smoothed with a 3×3 boxcar to remove statistical noise, and the calculations were done only for those pixels with significant count rates, $> 3\sigma$, in both lines. It is difficult to obtain a meaningful, quantitative estimate of the error in the map temperatures and emission measures other than to note that they are expected to be larger than at the Fe XVII peak (Table 1).

2.3 Beijing Magnetogram

Figure 1d shows a photospheric longitudinal magnetogram of AR 4906 on 18 December 1987, obtained from the Beijing Observatory (courtesy of H. Zhang and H. Wang). The sunspot is the oval-shaped pair of solid contours to the right of map center. The maximum line-of-sight umbral magnetic field strength is ~ 2600 G, and the noise level is ~ 100 G. Comparison of the umbral field strength with data taken at the Mt. Wilson Observatory shows good agreement, indicating that the magnetogram did not saturate. Just left (east) of the sunspot is a nearby region of opposite polarity with a maximum, inward directed field of ~ 790 G. Farther to the left is the trailing plage with a maximum, inward field of ~ 930 G.

Figure 1d also shows field lines obtained with the potential field extrapolation code developed by Sakurai (1982); this code solves Laplace's equation to calculate current-free magnetic field lines using the line-of-sight photospheric fields as boundary conditions. A cluster of field lines in the lower left portion of the sunspot terminates in and around the nearby, relatively strong region of opposite polarity. These field lines outline a loop-like structure (or bundle of loops) which is quite asymmetric. For several representative field lines, we list pairs of total extrapolated photospheric magnetic field strengths (in Gauss), where the first element corresponds to the footpoint inside the sunspot and the second to the footpoint in the region of opposite polarity: (1800,33), (1500,280), (1400,550). The corresponding photospheric footpoint separations for the above field lines are 5.06, 4.64, and 3.80×10^4 km.

3 Results

3.1 Analysis of the Sunspot

The Sakurai code was modified to obtain the total extrapolated magnetic field strength in a grid of locations all at the same specified height above the photosphere. Contour maps at heights of 0, 5000, 10000, and 15000 km are shown in Figure 3. The vertical gradient of the total magnetic field strength near the center of the umbra for heights between 0 and 5000 km is ~ 0.30 G/km. (This

is less than but comparable to the gradient of $0.41 - 0.67$ G/km obtained by Henze et al., 1982, for the longitudinal magnetic field in the transition region and photosphere of a sunspot umbra.) The average horizontal gradient in the total photospheric magnetic field strength is ~ 0.11 G/km. Knowing the height variation of the maximum total extrapolated sunspot field and assuming that this field can be described by that of a vertically oriented point dipole buried below the photosphere, we obtain a depth of 1.76×10^4 km and a dipole moment of 7.45×10^{15} G-km³.

These dipole parameters are used to calculate contours of constant magnetic field strength which extend well into the corona. Figure 4 shows magnetic field contours corresponding to the 1st through 5th harmonics of 1665 MHz and 4900 MHz. The dipole field is compared with the field calculated with the Sakurai code. Specifically, the radii in the x-direction of several field strength contours in the point dipole field (Fig. 4) were compared with the radii of these same contours in the four extrapolated maps of Figure 3. At these four heights, the corresponding contour radii are equal to better than 10% for magnetic fields $\gtrsim 300$ G and we find that the point dipole field is a good approximation of the extrapolated potential field within this three-dimensional structure; this approximation simplifies the calculation of microwave emission from sunspot models. For locations in which $B < 300$ G, nearby pockets of magnetic field perturb the sunspot field from that of a point dipole.

Figure 5 shows the theoretical I and V maps for 1665 MHz and 4900 MHz obtained using the point dipole approximation and the model sunspot atmosphere described in Brosius and Holman (1989). The failure of this simple model to reproduce the sunspot microwave structure provides insight into the temperature, density, and field structure above the sunspot: 1) The coronal temperature and/or density must be relatively low over large portions of the sunspot and 2) the microwave emission must emanate from some coronal structure other than the sunspot in order to explain the observed 6 and 20 cm I and V structure. The loop-like structure is explored in the next sub-section.

An overlay of the intensity maps in the 20 cm waveband (Fig. 2) with the magnetogram reveals that the 20 cm intensity contours do not cover the entire sunspot. The potential field extrapolations (Fig. 3) show that magnetic fields which are high enough to produce 2nd harmonic gyroemission at all four frequencies in the 20 cm waveband (245 - 297 G) occur at heights of 5000 - 15000 km, where coronal temperatures ($> 10^6$ K) and densities ($\sim 10^9$ cm⁻³) are expected to persist (Papagiannis and Kogut 1975, Hildebrandt et al. 1987). Indeed, 2nd harmonic gyroemission is expected to emanate from the portion of the sunspot for which the observed brightness temperature is less than the lowest observed intensity contour (5.3×10^5 K). Ways to obtain brightness temperatures this low from the 2nd harmonic gyroemission mechanism are 1) the density in the emission region is extremely low ($< 10^5$ cm⁻³ for a 2×10^6 K plasma), 2) the temperature in the emission region is less than 5.3×10^5 K, or 3) both the temperature and the density in the emission region are low. To obtain a density less than 10^5 cm⁻³ in the corona over a large fraction ($\sim 1/3$) of a sunspot area seems unlikely, but it cannot be ruled out. Thus we find that a lower temperature and/or density exists over a portion of both the sunspot umbra and penumbra on the side of the sunspot away from the center of AR 4906. This is consistent with the results of Gary and Hurford (1987) and with Strong, Alissandrakis, and Kundu (1984).

3.2 Analysis of the Loop Structure Connecting the Sunspot with the Nearby Region of Opposite Polarity

An overlay of the intensity maps in the 20 cm waveband (Fig. 2) with the magnetogram field lines (Fig. 1d) reveals that the peak of the sunspot-associated source in all four of the 20 cm intensity maps lies along the loop structure joining the sunspot with the nearby region of opposite polarity. Figure 6 shows the locations of the centers of the 20 cm peak intensity contours, along with the 6 cm I and V sources, on the magnetogram. The higher the frequency, the farther down the leg of the loop (on the side of the sunspot) the intensity peak occurs. Assuming the emission in the 20 cm peaks to be dominated by 2nd harmonic gyroemission, we estimate a magnetic field gradient ~ 0.0068 G/km along the loop in the plane of the sky. Assuming 3rd harmonic, the field gradient is ~ 0.0047 G/km. Both of these gradients are factors of 2 to 3 less than the gradients calculated along the individual extrapolated field lines which pass through the 20 cm emission peaks. Based upon the potential field extrapolation, the 20 cm peak emission region is comprised of a superposition of 2nd and 3rd harmonic gyroemission arising from the loop structure. The magnetic field strength ranges from 160 to 300 G in the 20 cm source region.

The 6 cm emission originates farther down the leg of the loop (on the side toward the sunspot) since much higher fields are required for gyroresonance emission at 6 cm than at 20 cm. The polarization structure shows two V sources – one on either side of the I source – such that the I and V sources all lie roughly along the length of the loop. The polarization is $\sim 60\%$ close to the edges of the I source. Such structure appears in the microwave loop models of Holman and Kundu (1985) and arises from the gyroresonance emission mechanism: the ordinary mode (O-mode) of a given harmonic becomes optically thin toward the harmonic edge more rapidly than does the extraordinary mode (X-mode). Assuming the emission in the 6 cm peak to be dominated by 3rd harmonic gyroemission (see next paragraph), we estimate an average magnetic field gradient (between the 6 and 20 cm source regions) ~ 0.020 G/km along the loop in the plane of the sky. This is less than but comparable to the average field gradient ~ 0.028 G/km calculated along the individual extrapolated field lines which pass through the 6 and 20 cm emission peaks.

In principle, the harmonic number of the 6 cm emission can be determined by comparing the observations with models. Although a simple dipole loop model does not accurately portray the asymmetry of the extrapolated field lines, we are only interested in reproducing the emission from one leg of the loop (the sunspot side of the loop in Fig. 6; the right half of Figure 7), so the magnetic field structure of the loop elsewhere is of little consequence. The density is selected so that the brightness temperature calculated for the portion of the loop away from the desired 6 cm source remains less than the lowest observed 6 cm brightness temperature contour, as observed. Both thermal bremsstrahlung and thermal gyroemission were included in the calculations and theoretical I and V maps at 6 cm were produced for three cases where the 2nd, 3rd, and 4th harmonic emission region was in the footpoint at a height of ~ 5000 km. The 6 cm I and V structure and magnitude could not be produced with 4th harmonic emission. For 2nd harmonic, the density required is low: $\sim 5 \times 10^6$ cm $^{-3}$. If the density were higher, the overlying 3rd harmonic emission region would yield too high a brightness temperature from a large area of the loop and would destroy the desired V structure. For 3rd harmonic, the density is $\sim 10^9$ cm $^{-3}$. This is reasonable in light of the sunspot atmosphere model of Hildebrandt et al. (1987) where a density of $\sim 8 \times 10^8$ cm $^{-3}$ occurs ~ 5000 km above the photosphere. The emission measure for the model loop with density $\sim 10^9$ cm $^{-3}$ is $\sim 10^{27}$ cm $^{-5}$, less than but comparable to the value of $\sim 10^{28}$ cm $^{-5}$ estimated from the very weak

Fe XVII flux measured by XRP at the location of the 6 cm source (and assuming $T_e = 2.5 \times 10^6$ K). The corresponding value for the model loop with density $\sim 5 \times 10^8 \text{ cm}^{-3}$ is $\sim 2 \times 10^{22} \text{ cm}^{-5}$, substantially less than the observed value. Thus our model, combined with XRP observations, indicates that the observed 6 cm I and V structure is indeed due to 3rd harmonic gyroemission. Accounting for the four frequencies at which the 6 cm emission was observed, this translates into magnetic field strengths ranging from 547 G to 583 G. At the location of the 6 cm source the potential field extrapolation yields a field ~ 600 G at a height ~ 5000 km, consistent with our deduced values.

These magnetic field and density results can be used to estimate the Alfvén speed and its variation within the loop. The magnetic field strength required for the highest frequency source in the 6 cm band, 583 G, gives an electron gyrofrequency of 1.63 GHz. The 6 cm source model is consistent with the observations when the electron density is between $5 \times 10^8 \text{ cm}^{-3}$ and $2 \times 10^9 \text{ cm}^{-3}$, giving a plasma frequency of 0.2 – 0.4 GHz. Hence, the ratio of the gyrofrequency to the plasma frequency is found to be in the range 4 – 8 and the Alfvén speed falls within the 28,000 – 57,000 km/sec range. (The estimated density of $1 \times 10^9 \text{ cm}^{-3}$ gives an Alfvén speed of 40,000 km/sec.) The 160 G – 300 G range for the magnetic field strength in the 20 cm source region gives an electron gyrofrequency ranging from 0.45 GHz to 0.84 GHz. The electron density is not as well established. With an estimated value of $1 \times 10^9 \text{ cm}^{-3}$, the ratio of the gyrofrequency to the plasma frequency ranges from 1.5 to 3, and the Alfvén speed ranges from 10,000 km/sec to 20,000 km/sec. Hence, the Alfvén speed in this coronal loop is highest near the sunspot and decreases toward the apex of the loop.

In wave heating theories of the corona, the heating rate is proportional to the Alfvén speed and the square of the wave velocity amplitude. The Alfvén speeds derived here are significantly greater than the generally quoted value of 1000 – 2000 km/s. This implies that the same heating rate can be achieved with a smaller wave amplitude. However, for resonant waves in a loop (as in resonant absorption theories), the period of the driving wave must be shorter. For a loop length of 100,000 km and an Alfvén speed of 20,000 km/sec, the wave period must be 10 sec or less. Moreover, the gyrofrequency is generally assumed to be less than the plasma frequency, the opposite of what is found here and in other CoMStOC results. The value of this ratio determines which plasma instabilities are important.

At the location of the 6 cm peak, where the brightness temperature is $\sim 2.5 \times 10^6$ K, the 20 cm brightness temperature is lower, $\sim 1.3 \times 10^6$ K. Because lower frequencies require lower fields for the thermal gyroemission mechanism and, because the magnetic field diminishes with increasing height in the atmosphere, the 20 cm emission must originate higher in the atmosphere than the 6 cm emission. Indeed, fields high enough for 20 cm 2nd harmonic gyroemission (245 – 297 G) occur over the 6 cm source at heights in excess of 15,000 km. If the brightness temperature is $\sim 1.3 \times 10^6$ K and the 2nd harmonic is optically thin, the 20 cm emission should be polarized since the O-mode is less optically thick than the X-mode. This polarization is not observed and we conclude that the observed 20 cm brightness temperature is due to optically thick 2nd harmonic gyroemission in a region where $T_e \sim 1.3 \times 10^6$ K. This means that the plasma temperature at the height of formation of the 6 cm emission is higher than the plasma temperature at the height of formation of the 20 cm emission. Thus, at the location of the 6 cm intensity peak, the plasma temperature *diminishes with height*.

3.3 Analysis of the Plage

The electron temperature and column emission measure values obtained from the XRP data can be used to compute the thermal bremsstrahlung microwave emission from the X-ray emitting plasma. The optical depth due to thermal bremsstrahlung (free-free) absorption is

$$\tau_{ff}^{X,O} = \frac{9.786 \times 10^{-21} (EM) \ln(47T_e/\nu)}{n_\nu T_e^{1.5} (\nu \mp \nu_B \cos \theta)^2}, \quad (1)$$

where T_e is the electron temperature in K, EM is the emission measure in cm^{-5} , ν is the observation frequency in GHz, n_ν is the index of refraction (~ 1 for plasma and field conditions here), ν_B is the electron gyrofrequency ($\nu_B = 2.8 \times 10^{-3} B$, where B is in Gauss and ν_B is in GHz), θ is the angle between the field and the line of sight, and the minus sign refers to X-mode while the plus sign refers to O-mode. The thermal bremsstrahlung brightness temperature predicted for each mode can be calculated using

$$T_{B;X,O}^{PRED} = T_e^2 [1 - \exp(-\tau_{ff}^{X,O})]. \quad (2)$$

In a magnetized plasma, the optical depth, and hence the predicted brightness temperature, of the X-mode emission is expected to be higher than that of the O-mode. The predicted total intensity I^{PRED} is simply the average brightness temperature of the two modes which, depending on the direction of the magnetic field, are associated with right circular polarized (RCP) or left circular polarized (LCP) emission.

At the location of the Fe XVII peak, where the XRP spectroscopic scan data used to generate Table 1 were obtained, the electron temperature of the plasma observed by XRP was $2.95 \pm 0.20 \times 10^6$ K and the log of the column emission measure was 28.85 ± 0.19 . These values entered into the equations above yield the predicted intensities listed in Table 2. The uncertainties are due to the errors associated with the electron temperature and emission measure values in Table 1. At this same location in the plage, the VLA observed an intensity $I_{20}^{OBS} \sim 1.2 \times 10^6$ K at all four frequencies in the 20 cm waveband, and $I_6^{OBS} < 0.42 \times 10^6$ K in the 6 cm waveband. Our predicted intensities in the 6 cm waveband are all consistent with the VLA observations. Our predicted intensities in the 20 cm waveband are about 1.4 to 1.9 times higher than the corresponding observed intensities. Thus it appears that thermal bremsstrahlung plays a significant role in the observed plage emission.

The picture becomes considerably more complex when the observed polarization is considered. Table 2 lists the observed intensity and the LCP and RCP brightness temperatures ($T_{B,L}^{OBS}$ and $T_{B,R}^{OBS}$) for each of the four frequencies in the 20 cm waveband at the location of the XRP spectroscopic scan. The X-mode corresponds to the RCP emission for outward directed fields, and to the LCP emission for inward directed fields; the O-mode corresponds to the LCP emission for outward directed fields and to the RCP emission for inward directed fields. The LCP emission is reasonably consistent with the predicted thermal bremsstrahlung brightness temperature (I^{PRED}). However, the observed RCP emission is considerably lower, by a factor of 2 to 4, than the predicted value. Thus, some mechanism is required to explain the reduction of the expected RCP emission to its observed value. The only way to reduce the expected brightness temperatures of $\sim 2 \times 10^6$ K to the observed value $\sim 7 \times 10^5$ K is to have cooler absorbing plasma along the line of sight between the emission region and the observer.

One possible model which explains the discrepancy between the observed and the predicted polarization is that the source region consists of two layers of hot plasma separated by an inter-

vening layer of cooler plasma. The lowest layer contains the highest column emission measure and, therefore, is responsible for the majority of both the X-ray emission and the predicted thermal bremsstrahlung microwave emission. The intervening layer of cooler plasma absorbs out the microwave emission from this lower hot layer, leaving only the microwave emission from the uppermost hot layer to be detected by the VLA (see Figure 8a). The uppermost hot layer, optically thin to thermal bremsstrahlung, is embedded in a magnetic field such that thermal gyroemission, capable of producing the observed high polarization, produces the observed 20 cm microwave emission. The cool intervening layer must have a temperature $\leq 5 \times 10^5$ K in order to reduce the predicted RCP emission at 1665 MHz from 1.75×10^6 K to its observed value of 5×10^5 K. If, for example, the cool absorbing plasma has a temperature of 10^5 K, it needs $\log EM = 27.5$ to get $\tau_{ff} \sim 5$ at 1665 MHz. This means that if the cool absorbing layer forms a sheath ~ 3500 km thick, it needs a reasonable density $\sim 3 \times 10^9 \text{ cm}^{-3}$ in order to be an effective absorber. If gyroabsorption contributes to the opacity of this cool layer, the required emission measure may be lower. In order for the uppermost hot layer to both emit strongly in the 20 cm waveband and produce polarization as high as $\sim 50\%$, the layer must contain magnetic fields sufficiently high for gyroemission. From our potential field extrapolation at and near the location of the XRP spectroscopic scan, we find that the requisite magnetic field strengths are present, indicating that the observed 20 cm emission could originate in a gyroresonance emission layer between heights of ~ 5000 and $\sim 15,000$ km. Since the radiation is emitted primarily in the X-mode and the longitudinal field direction is inward, the emitted radiation will be LCP, as observed (Figure 2).

Plasma and magnetic field parameters in the uppermost hot layer can be calculated. The optical depth of the uppermost hot layer $\tau_{UH}^{X,O}$ can be estimated by solving

$$T_B^{X,O} = T_c \exp(-\tau_{UH}^{X,O}) + T_e [1 - \exp(-\tau_{UH}^{X,O})] \quad (3)$$

for $\tau_{UH}^{X,O}$, where $T_B^{X,O}$ are the observed X- (LCP) and O- (RCP) mode brightness temperatures at a particular frequency, T_c is the brightness temperature of the optically thick, underlying cool absorbing plasma ($T_c \leq 5 \times 10^5$ K), and T_e is the electron temperature of the uppermost hot layer ($T_e > 2 \times 10^6$ K). Solving for $\tau_{UH}^{X,O}$ we obtain

$$\tau_{UH}^{X,O} = \ln[(T_e - T_c)/(T_e - T_B^{X,O})]. \quad (4)$$

Assuming $T_e = 3 \times 10^6$ K and $T_c = 1 \times 10^5$ K, we obtain $\tau_{UH}^X = 0.80$ and $\tau_{UH}^O = 0.15$ for the observed brightness temperatures at 1665 MHz. Now the optical depth due to gyroresonance absorption can be written (e.g., Kundu 1965, Zheleznyakov 1970)

$$\tau_{gr}^{X,O} = 0.052 \frac{s^{2s}}{2^{s+1}s!} n_e \nu^{-1} L_B (1.77 \times 10^{-10} T_e)^{s-1} (1 \pm \cos \theta)^2 \sin^{2s-2} \theta, \quad (5)$$

where s is the harmonic number, n_e is the electron density, ν is the frequency, L_B is the magnetic scale height ($B/\nabla B$), T_e is the electron temperature, θ is the angle between the field and the line of sight, and the plus sign refers to X-mode while the minus sign refers to O-mode. The ratio

$$\tau_{UH}^X / \tau_{UH}^O = (1 + \cos \theta)^2 / (1 - \cos \theta)^2 \quad (6)$$

yields the angle between the field and the line of sight which is required in order to produce the calculated X- and O-mode optical depths in the upper hot layer. For the case discussed above, the calculated angle is 66° , comparable to the angle obtained from the extrapolated coronal magnetic field.

The magnetic scale height L_B can also be calculated from the potential field extrapolation. It is 0.94×10^9 cm in the 2nd harmonic gyroemission region, 1.4×10^9 cm in the 3rd, and 1.8×10^9 cm in the 4th. Using $\tau_{UH}^X \sim 0.8$, $T_e = 3 \times 10^6$ K, $\nu \sim 1500$ MHz, and $\theta \sim 60^\circ$, we calculate the electron density n_e required in the upper hot layer if the emission process is due to 2nd harmonic gyroemission ($n_e = 3.0 \times 10^4$ cm $^{-3}$), 3rd harmonic gyroemission ($n_e = 6.8 \times 10^6$ cm $^{-3}$), and 4th harmonic gyroemission ($n_e = 1.2 \times 10^9$ cm $^{-3}$).

A second possible model consists of two layers of plasma: the lower hot layer seen by XRP and a cooler overlying layer where gyroresonance absorption takes place. In this cool absorbing layer, neither mode is optically thick and since the X-mode is more attenuated than the O-mode, the resulting emission is dominated by O-mode. The observed emission, however, seems to be X-mode (it is left-circularly polarized, with an inward-directed underlying photospheric field). Nevertheless, the microwave emission can undergo a polarization inversion upon traversing a "quasi-transverse" (QT) layer in the coronal magnetic field (see Fig. 8b). This QT layer occurs where the magnetic field becomes transverse to the line of sight, i.e., the longitudinal field component B_z becomes zero. Previous studies have provided evidence for such polarization inversion (Kundu et al. 1977, Webb et al. 1983, Alissandrakis and Kundu 1984). The observed polarization is inverted when coupling between the polarization modes is weak.

Zheleznyakov (1970), using the WKB method, obtains the following expression for the coupling parameter, given here in the notation of Bandiera (1982):

$$C = \frac{2 \ln 2}{\pi^2} \frac{(m_e c)^4}{e^5} \frac{\omega^4}{N_e B^3} \left| \frac{d\theta}{ds} \right|, \quad (7)$$

where m_e and e are the rest mass and charge on an electron, c is the speed of light, ω is the observation angular frequency, N_e is the electron number density, B is the magnetic field strength, and $d\theta/ds$ is the gradient of the angle between the field and the line of sight; all units are in CGS. The microwave emission undergoes a polarization inversion when $C \ll 1$, or

$$4.766 \times 10^{-18} \frac{\nu^4}{N_e B^3} \left| \frac{d\theta}{ds} \right| \ll 1. \quad (8)$$

In and near the location of the XRP spectroscopic scan, the Sakurai code yields a QT layer at a height of $\sim 75,000$ km. The average total magnetic field strength obtained from the code is 17 G, and the angular gradient along the line of sight is 1.1×10^{-10} rad/cm. Inserting these values into the expression for the coupling parameter and using the highest observing frequency in the 20 cm waveband (1.665 GHz), we find that the polarization inversion will take place if the electron density in the QT layer exceeds 8.4×10^5 cm $^{-3}$. The model plage electron density of Hildebrandt et al. (1987) at a height of 75,000 km is 1.4×10^9 cm $^{-3}$, and the model electron densities in all of the coronal structures in Hildebrandt et al. (1987) and Pagagiannis and Kogut (1975) exceed 5.4×10^7 cm $^{-3}$ at the same height. Thus it is reasonable to expect polarization inversion to occur for the 20 cm microwave emission from the plage: the 20 cm emission exiting the cool absorbing plasma, dominated by the O-mode (RCP), is inverted in the QT layer so that the O-mode emission becomes LCP, as observed.

Plasma and magnetic field parameters in the cool absorbing layer can be calculated. The optical depths of the cool absorbing layer $\tau_c^{X,O}$ can be estimated by solving

$$T_B^{X,O} = T_B^{PRED} \exp(-\tau_c^{X,O}) + T_c[1 - \exp(-\tau_c^{X,O})] \quad (9)$$

for $\tau_c^{X,O}$, where $T_B^{X,O}$ are the observed X- and O- mode brightness temperatures at a particular frequency (prior to polarization inversion), T_B^{PRED} is the brightness temperature due to thermal bremsstrahlung predicted from the X-ray observations, and T_e is the electron temperature of the cool absorbing layer. Solving for $\tau_c^{X,O}$ we obtain

$$\tau_c^{X,O} = \ln[(T_e - T_B^{PRED})/(T_e - T_B^{X,O})]. \quad (10)$$

For the average observed brightness temperatures in the 20 cm waveband, we obtain $\tau_c^X = 1.44$ and $\tau_c^O = 0.18$ for $T_e = 3 \times 10^5$ K, which leads to $\theta \sim 62^\circ$. This angle is comparable to the angle obtained from the extrapolated field. Using $\tau_c^X \sim 1.44$, $T_e = 3 \times 10^5$ K, $\nu \sim 1500$ MHz, and $\theta \sim 60^\circ$, we calculate the electron density n_e required in the cool absorbing layer if the absorption process is due to 2nd harmonic gyroabsorption ($n_e = 5.5 \times 10^5 \text{ cm}^{-3}$), 3rd harmonic gyroabsorption ($n_e = 1.2 \times 10^9 \text{ cm}^{-3}$), and 4th harmonic gyroabsorption ($n_e = 2.1 \times 10^{12} \text{ cm}^{-3}$). The 2nd-harmonic density is considerably less than canonical low coronal density values, but cannot be ruled out. The 3rd-harmonic density is consistent with canonical low coronal density values, and is also consistent with the density requirement for polarization inversion in the QT layer (although the QT layer is $\sim 70,000$ km higher in the atmosphere). The 4th-harmonic density is so high that plasma suppression would prohibit the propagation of 20 cm electromagnetic radiation, so this can be ruled out. The absorption which produces the observed polarization at the location of the XRP spectroscopic scan most likely occurs in the 3rd harmonic gyroresonance absorption region.

The situation is somewhat different at the location of the 20 cm intensity peak in the plage. Here, $\sim 30,000$ km west of the location of the XRP spectroscopic scan, the predicted and the observed 20 cm intensity peaks are cospatial. The predicted brightness temperature is 2.2×10^6 K, while the observed LCP brightness temperature is 1.9×10^6 K and the observed RCP brightness temperature is 0.9×10^6 K. The maximum predicted 6 cm brightness temperature is 7×10^5 K, while the observed is $< 4.2 \times 10^5$ K. This, again, requires the presence of cooler absorbing plasma overlying the hot plasma observed by XRP. Here, however, the coronal potential field is not sufficient for the gyroemission mechanism to operate. The photospheric field is less than 100 G, and between heights of 5000 and 15,000 km the total extrapolated field ranges from ~ 60 to ~ 90 G. This suggests quite strongly that the extrapolated field is substantially less than the actual magnetic field in the corona. This is possibly a manifestation of instrumental insensitivity to photospheric longitudinal magnetic fields less than ~ 100 G. It is quite possible that compact, highly intense photospheric magnetic field regions were not detected due to inadequate instrumental resolution. It also cannot be ruled out that electric currents, and hence non-potential magnetic fields, are present in the corona.

These models represent the two simplest ways to describe and interpret the simultaneous, multi-waveband data taken of AR 4906. Simpler models can, of course, explain the microwave images, the X-ray spectra, or the magnetic extrapolations individually or even explain any two of these, but the two models explained in detail above and depicted in Figure 8 can describe the entire data set.

4 Conclusions

A number of important conclusions concerning the plasma and magnetic field structure of an active region, as well as the observational methods, result from this study:

(1) The temperature in the corona over an active region can diminish with height; this occurs over both the sunspot and the plage in AR 4906 where a different line of reasoning leads to this conclusion for each structure. In the case of the sunspot, the cospatial microwave emission in the 6 and 20 cm wavebands have substantially different brightness temperatures. The emission in both wavebands is attributed to optically thick thermal gyroemission in the high magnetic field of the sunspot. The 6 cm emission requires higher fields than the 20 cm emission and, hence, originates lower in the sunspot atmosphere. Where the 6 and 20 cm emission overlap, the 6 cm brightness temperature is 2.5×10^6 K while the 20 cm brightness temperature is 1.3×10^6 K. Thus the sunspot atmospheric temperature diminishes from 2.5×10^6 K at the height of the 6 cm emission to 1.3×10^6 K at the height of the 20 cm emission. In the case of the plage, the conclusion is based upon the discrepancy between the observed RCP emission at 20 cm and the brightness temperature predicted from the XRP line flux ratios. Specifically, this requires the presence of overlying cool, absorbing plasma in order to reduce its predicted brightness temperature of $T_B^{PRED} \sim 2 \times 10^6$ K to its observed value of $T_{B,R}^{OBS} \sim 0.7 \times 10^6$ K. The overlying, cool plasma must have a temperature $\leq 5 \times 10^5$ K.

(2) A loop or loop-like structure connects the sunspot with a nearby region of opposite polarity in the east. The peaks of the 6 and 20 cm emission lie along this loop, with higher frequency emission originating farther down the leg of the loop on the side of the sunspot. Based upon the potential field extrapolation, the 20 cm emission is due to a combination of 2nd and 3rd harmonic gyroemission, putting the magnetic field strength in this region in the range 160 – 300 G.

(3) Based upon a comparison of the 6 cm and X-ray observations with calculations of the emission from a model loop, we deduced the plasma and magnetic field parameters at the location of the 6 cm source. An electron temperature $T_e = 2.5 \times 10^6$ K, an electron density $N_e \sim 1 \times 10^9$ cm⁻³, and a magnetic field strength of 583 G (3rd harmonic gyroemission at 4900 MHz) result. The potential field extrapolation yields this magnetic field strength at a height ~ 5000 km above the photosphere.

(4) These results have allowed us to obtain good estimates of the Alfvén speed at two locations within the loop. At the 6 cm source near the sunspot, an Alfvén speed $\sim 40,000$ km/sec is obtained. Higher in the loop, at the location of the 20 cm emission, the Alfvén speed is found to range from 10,000 km/sec – 20,000 km/sec. These values are substantially higher than the 1000 – 2000 km/sec typically quoted for the Alfvén speed in the corona. At both locations the electron gyrofrequency exceeds the plasma frequency.

(5) The extrapolated potential sunspot field can be approximated by that of a vertically oriented point dipole for locations in which $B \gtrsim 300$ G. For locations in which $B < 300$ G, nearby pockets of magnetic field perturb the sunspot field from that of a point dipole.

(6) The electron temperature and/or density are lower over the western portion of the sunspot (away from the center of the active region) than they are over the eastern portion of the sunspot.

(7) In the plage, the ratios of X-ray emission lines are used to calculate the electron temperature and column emission measure. The most accurate determination of these parameters is at the location of the Fe XVII peak flux, where spectroscopic scan data were obtained. The Fe XVII emissivity needs to be divided by a correction factor ~ 2.75 . This is somewhat higher than but comparable to the ~ 2.25 factor obtained in CoMStOC I.

(8) The predicted 20 cm brightness temperature in the plage is reasonably consistent with the observed for the LCP emission but is much higher for the RCP emission. We have proposed two possible models to explain this discrepancy. Both models are as simple as possible yet still incorporate all three sets of data for AR 4906: The first model has a low layer of hot plasma (where the X-ray emission originates) covered by an optically thick cool, absorbing layer. On top of this cool plasma is a second hot layer which is optically thin to thermal bremsstrahlung but emits strong, polarized microwave emission since it is embedded in a magnetic field sufficient for gyroresonance emission at 20 cm. Since the longitudinal component of the magnetic field inverts at a height of $\sim 75,000$ km, the density at this height cannot exceed $\sim 8 \times 10^5 \text{ cm}^{-3}$; otherwise, the polarization will invert in this QT layer and the sense of polarization will be opposite that observed. (It should be pointed out that the model coronal densities of Hildebrandt et al., 1987, and Papagiannis and Kogut, 1975, greatly exceed $8 \times 10^5 \text{ cm}^{-3}$ at a height of 75,000 km.) The second model has a layer of cool, but not fully thick, absorbing plasma overlying the hot plasma from which the predicted microwave emission originates. This cool plasma, embedded in a magnetic field sufficient for gyroresonance absorption, attenuates the X-mode more strongly than the O-mode. The polarization is subsequently inverted in the overlying QT layer in the magnetic field. Appropriate coronal magnetic field strengths, as well as the QT layer, are extrapolated from the photospheric longitudinal magnetogram with the Sakurai (1982) code. A similar result has been obtained from the analysis of the CoMStOC II data (Schmelz et al. 1991).

(9) Elsewhere in the plage, at the observed 20 cm intensity peak, we find that the magnetic field required to explain the observations is higher than the coronal potential field extrapolated from the photospheric longitudinal magnetogram. A similar discrepancy has been found in the analysis of other CoMStOC data.

Acknowledgements. We gratefully acknowledge the assistance of Dr. Haimin Wang in the acquisition of the Beijing Observatory magnetogram. Radio astronomical studies of the Sun at Tufts University are supported under grant AFOSR-89-0147 with the Air Force Office of Scientific Research. Simultaneous VLA and SMM observations of the Sun are supported by NASA grant NAGW-2383 to Tufts University. JTS acknowledges support by NASA contracts NAS5-30431 and NAS5-28713 and the Lockheed Independent Research Program. JWB and GDH acknowledge support by the SMM Guest Investigator Program and NASA RTOP 170-38-53-16. The success of the SMM CoMStOC observations depended on the efforts of many persons at the SMM Experimenters Operations Facility. The VLA is operated by Associated Universities Inc., under contract with the National Science Foundation. The XRP data used in this work were available only because of the repair of the SMM spacecraft by the crew of the Challenger on mission 41-C. The pilot for that mission, and the commander of Challenger's last flight, was Francis R. Scobee. This work is dedicated to his memory.

TABLE 1
Plasma Parameters from XRP Spectroscopic Scan Data

<u>Line Ratio</u>	<u>T_e (MK)⁽¹⁾</u>	<u>$\log(\text{EM})$ (cm⁻⁵)⁽²⁾</u>
O VIII/Mg XI	3.01 ± 0.16	28.85 ± 0.08
O VIII/Fe XVIII	2.83 ± 0.19	28.87 ± 0.09
Ne IX/Fe XVIII	2.94 ± 0.22	28.85 ± 0.09
Mg XI/Fe XVIII	2.61 ± 0.50	28.89 ± 0.24
Fe XVII/Fe XVIII	3.12 ± 0.27	28.83 ± 0.06
weighted mean ⁽³⁾	2.95 ± 0.20	28.85 ± 0.19

(1) The quoted uncertainties on the individual values of T_e reflect counting statistics only.

(2) The column emission measure is computed from the O VIII flux only; the quoted uncertainties on the individual values reflect counting statistics only.

(3) The quoted uncertainties on the weighted means of T_e and EM are the root mean squares of the statistical and systematic uncertainties. For temperature, the systematic uncertainty is estimated as the standard deviation of the individual values. For the emission measure, the systematic uncertainty is estimated as the standard deviation of the emission measures calculated for the O VIII, Ne IX, Mg XI, and Fe XVIII fluxes at the mean T_e .

TABLE 2
Predicted Microwave Intensities from XRP Spectroscopic Scan Data And Observed Microwave
Intensities from the VLA

<u>Freq. (MHz)</u>	<u>I^{PRED} (MK)</u>	<u>I^{OBS} (MK)</u>	<u>$T_{B,L}^{OBS}$ (MK)</u>	<u>$T_{B,R}^{OBS}$ (MK)</u>
1375	2.17 ± 0.49	1.2	1.5	0.9
1420	2.10 ± 0.49	1.1	1.5	0.7
1550	1.91 ± 0.49	1.4	2.0	0.8
1665	1.75 ± 0.49	1.1	1.7	0.5
4600	$0.31^{+0.17}_{-0.11}$	<0.42	—	—
4700	$0.30^{+0.16}_{-0.11}$	<0.42	—	—
4800	$0.29^{+0.16}_{-0.10}$	<0.42	—	—
4900	$0.28^{+0.15}_{-0.10}$	<0.42	—	—

References

- Acton, L. W., et al. 1980, *Solar Phys.*, **65**, 53.
- Alissandrakis, C. E., and Kundu, M. R. 1982, *Ap. J. (Letters)*, **253**, L49.
- Alissandrakis, C. E., and Kundu, M. R. 1984, *Astr. Ap.*, **139**, 271.
- Bandiera, R. 1982, *Astr. Ap.*, **112**, 52.
- Bastian, T. 1987, Ph.D. thesis, University of Colorado.
- Brosius, J. W., and Holman, G. D. 1988, *Ap. J.*, **327**, 417.
- Brosius, J. W., and Holman, G. D. 1989, *Ap. J.*, **342**, 1172.
- Cornwell, T. 1986, in *Synthesis Imaging* (NRAO Summer School Course Notes), p. 117.
- Gary, D. E., and Hurford, G. J. 1987, *Ap. J.*, **317**, 522.
- Henze, W., Jr., Tandberg-Hanssen, E., Hagyard, M. J., Woodgate, B. E., Shine, R. A., Beckers, J. M., Bruner, M., Gurman, J. B., Hyder, C. L., and West, E. A. 1982, *Solar Phys.*, **81**, 231.
- Hildebrandt, J., Kruger, A., Urpo, S., and Terasranta, H. 1987, *Observation and Interpretation of Solar S-Component Radiation at Millimeter Waves* (Helsinki Univ. of Technology Radio Lab., Rept. S170).
- Holman, G. D., and Kundu, M. R. 1985, *Ap. J.*, **292**, 291.
- Kundu, M. R. 1965, *Solar Radio Astronomy* (New York: Interscience).
- Kundu, M. R., Alissandrakis, C. E., Bregman, J. D., and Hin, A. C. 1977, *Ap. J.*, **213**, 278.
- Lang, K. R., and Willson, R. F. 1982, *Ap. J. (Letters)*, **255**, L111.
- Lang, K. R., Willson, R. F., and Gaizauskas, V. 1983, *Ap. J.*, **267**, 455.
- Lang, K. R., Willson, R. F., and Rayrole, J. 1982, *Ap. J.*, **258**, 384.
- Lang, K. R., Willson, R. F., Smith, K. L., and Strong, K. T. 1987, *Ap. J.*, **322**, 1035.
- Lang, K. R., Willson, R. F., Smith, K. L., and Strong, K. T. 1987, *Ap. J.*, **322**, 1044.
- McConnell, D., and Kundu, M. R. 1983, *Ap. J.*, **269**, 698.
- Mewe, R., Gronenschild, E. H. B. M., and van den Oord, G. H. J. 1985, *Astr. Ap. Suppl.*, **62**, 197.

- Meyer, J.-P. 1985, *Ap. J. Suppl.*, **57**, 173.
- Nitta, N., White, S. M., Kundu, M. R., Gopalswamy, N., Holman, G. D., Brosius, J. W., Schmelz, J. T., Saba, J. L. R., and Strong, K. T. 1991, *Ap. J.*, **374**, 374 (CoMStOC I).
- Papagiannis, M. D., and Kogut, J. A. 1975, *Brightness Temperatures and Polarizations of Solar Active Regions at 3.8 cm - Theory and Observations* (AFCRL-TR-75-0430).
- Sakurai, T. 1982, *Solar Phys.*, **76**, 301.
- Schmahl, E. J., Kundu, M. R., Strong, K. T., Bentley, R. D., Smith, J. B., Jr., and Krall, K. R. 1982, *Solar Phys.*, **80**, 233.
- Schmelz, J. T., Holman, G. D., Brosius, J. W., and Gonzalez, R. D. 1991, *Ap. J.*, in preparation (CoMStOC II).
- Shevgaonkar, R. K., and Kundu, M. R. 1984, *Ap. J.*, **283**, 413.
- Strong, K. T., Alissandrakis, C. E., and Kundu, M. R. 1984, *Ap. J.*, **277**, 865.
- Webb, D. F., Davis, J. M., Kundu, M. R., and Velusamy, T. 1983, *Solar Phys.*, **85**, 267.
- Webb, D. F., Holman, G. D., Davis, J. M., Kundu, M. R., and Shevgaonkar, R. K. 1987, *Ap. J.*, **315**, 716.
- Willson, R. F. 1985, *Ap. J.*, **298**, 911.
- Zheleznyakov, V. V. 1970, *Radio Emission of the Sun and Planets*, ed. J. S. Hey (Oxford: Pergamon Press).

Figure Captions

Figure 1. Observations of the CoMStOC IV active region, AR 4906. Celestial north is up, and west is to the right. All eight boxes cover the same field of view, for ease in coalignment. The tick spacing is one minute of arc, the crosses mark the locations of the phase center of the VLA observations, and "X" marks the location of the XRP spectroscopic scan. (a) Frequency-averaged map of I (intensity) at 20 cm. The contour levels are 0.21, 0.41, 0.62, 0.83, 1.03, 1.24, 1.45, 1.66, 1.86, and 2.07×10^6 K. (b) Frequency-averaged map of I at 6 cm. The contour levels are 0.42, 0.63, 0.84, 1.05, 1.26, 1.47, 1.68, 1.89, and 2.10×10^6 K. (c) XRP soft X-ray map of AR 4906 in the bright Fe XVII line at 15.01 Å. The image was accumulated during a 4' square raster with 10" steps which took 10 min to complete. The map has been smoothed with a 3 x 3 boxcar to improve statistics. Contour levels are 5, 10, 15, 20, 25, 30, 35, and 40 counts/s. (d) Photospheric longitudinal magnetogram obtained from the Beijing Observatory, with superimposed magnetic field lines calculated with the potential field extrapolation code of Sakurai. The contour levels are 200 and 500 G, where the dashed contours represent inward directed fields and the solid contours represent outward directed fields. (e) Electron temperature and (f) log of the column emission measure calculated from line flux ratios of emission lines observed with XRP. The contours in (e) are 2.2, 2.4, 2.6, 2.8, and 3.0×10^6 K; the contours in (f) are 28.7, 28.9, and 29.1. The temperature and emission measure diagnostics were available only in the plage. (g) Brightness temperature map at 20 cm calculated for the thermal bremsstrahlung emission mechanism using the electron temperature and column emission measure maps in (e) and (f). The contours are 1.7, 1.9, and 2.1×10^6 K. (h) Brightness temperature map at 6 cm calculated for the thermal bremsstrahlung emission mechanism using the electron temperature and column emission measure maps in (e) and (f). The contours are 0.1, 0.3, and 0.5×10^6 K.

Figure 2. I and V maps at each of the four frequencies in the 20 cm waveband. The I contour levels are 0.53, 0.79, 1.05, 1.31, 1.57, 1.83, 2.09, and 2.35×10^6 K for all frequencies. The V contour levels are 0.29 and 0.38×10^6 K at 1375 MHz; 0.27, 0.36, and 0.46×10^6 K at 1420 MHz; 0.31, 0.41, 0.51, and 0.61×10^6 K at 1550 MHz; and 0.40, 0.53, and 0.66×10^6 K at 1665 MHz. Celestial north is up, and west is to the right. The tick spacing is one minute of arc, and the crosses mark the location of the phase center of the VLA observations.

Figure 3. Sequence of contour maps showing the extrapolated magnetic field strength at heights of (a) 0 km, (b) 5000 km, (c) 10000 km, and (d) 15000 km above the photosphere. Celestial north is up, and west is to the right. The numbers along the axes are distances from solar disk center in units of 10^4 km in the plane of the sky. The contour levels in (a) and (b) are 150, 250, 350, 500, and 800 G. The contour levels in (c) and (d) are 150, 200, 250, 350, and 500 G. Crosshairs mark the phase centers of the VLA 6 and 20 cm maps, to assist in coaligning images. A 40" line segment is shown in (d) to assist in scaling and coaligning.

Figure 4. Magnetic field of a model sunspot consisting of a vertically oriented point dipole buried below the photosphere. Numbers along the x and y axes represent the distance from the point dipole in units of 10^4 km. The x-axis is in the plane of the photosphere, and the y-axis is perpendicular to that plane. Solid lines are field lines, dashed lines numbered 1 through 5 are contours of constant magnetic field strength, and the dotted horizontal lines represent heights above the photosphere of 5000, 10000, and 15000 km. In (a) the dashed lines are magnetic field contours corresponding to the 1st through 5th harmonics of 1665 MHz: 594, 297, 198, 149, and 119 G. In (b) the dashed lines are magnetic field contours corresponding to the 1st through 5th harmonics

of 4900 MHz: 1749, 875, 583, 437, and 350 G.

Figure 5. I and V maps calculated for 1665 MHz and 4900 MHz for the sunspot model whose magnetic field is shown in Figure 4. Numbers along the x and y axes are in units of arcsec, and the crosshairs intersect at the center of the sunspot. Contour line thickness increases with increasing contour value. In (a) the 1665 MHz I contours are 0.84, 1.37, and 1.90×10^6 K, and in (b) the 1665 MHz V contours are 0.27, 0.53, and 0.80×10^6 K. In (c) the 4900 MHz I contours are 0.66, 1.28, and 1.90×10^6 K, and in (d) the 4900 MHz V contours are 0.31, 0.62, and 0.93×10^6 K.

Figure 6. Portion of the magnetogram showing the locations of the 6 and 20 cm emission along the field lines which outline the loop-like structure connecting the sunspot with the nearby region of opposite polarity. Celestial north is toward the top, and west is toward the right. A segment of $10''$ length is shown for scaling purposes. Shaded areas show where the photospheric longitudinal field exceeds 200 G. The solid magnetic field contours represent outward directed fields of 200 and 500 G, while the short-dashed magnetic field contours represent inward directed fields of 200 and 500 G. The sunspot is the large shaded area in the upper right. The long-dashed contour corresponds to an intensity I of 0.79×10^6 K at the representative 20 cm microwave frequency of 1375 MHz. The "+" symbols mark the locations of the peak brightness temperature of each of the four closely-spaced frequencies in the 20 cm waveband. The location of the peak brightness temperature shifts systematically closer to the footpoint inside the sunspot with increasing frequency: the "+" farthest to the left corresponds to the 1375 MHz emission, and the "+" farthest to the right corresponds to the 1665 MHz emission. The dotted contour corresponds to an intensity I of 1.56×10^6 K at 4900 MHz in the 6 cm waveband. The dot-dash contours correspond to a V of 0.39×10^6 K at 4900 MHz.

Figure 7. Theoretical 4900 MHz I and V maps for the model loop described in the text. The height of the loop apex (16000 km), the footpoint separation (50000 km), and the loop thickness at the apex (7700 km) were all estimated from the extrapolated potential field lines. The cross section of the loop is taken to be circular at the apex. The model loop has a constant temperature of 2.5×10^6 K, a density of $1 \times 10^9 \text{ cm}^{-3}$, and a field strength of 583 G (3rd harmonic) in the footpoints at a height of ~ 5000 km above the photosphere. The I contours are 0.52, 1.04, 1.56, and 2.34×10^6 K. The V contours are 0.39, 0.52, 0.64, and 1.00×10^6 K. The model I and V sources on the right side of the figure reproduce the observed 6 cm I and V sources fairly well.

Figure 8. Illustration of the two models used to explain the observed polarization of the 20 cm microwave emission from the plage. The arrows labeled with an "R" correspond to RCP emission and the arrows labeled with an "L" correspond to LCP emission. The propagation mode is indicated by an "X" or an "O" in parentheses. The propagation mode is determined by the orientation of the local magnetic field, indicated by arrows labeled B_z . The lengths of the arrows labeled R and L indicate the relative brightness temperatures of the emergent emission in the given mode of polarization. (a) The hot/cool/hot layer model. Emission with high brightness temperature and low polarization ($T_B^{X,O} \sim 2 \times 10^6$ K) emerges from the lowest layer. This emission is then absorbed by the overlying cooler layer, from which low brightness temperature emission ($T_B^{X,O} < 5 \times 10^5$ K) emerges. Highly polarized emission ($T_B^X \sim 2 \times 10^6$ K, $T_B^O \sim 7 \times 10^5$ K) emerges from the highest layer, which is a hot plasma embedded in a magnetic field which is sufficiently strong for gyroresonance emission. (b) The hot/cool/QT layer model. Emission with high brightness temperature and low polarization ($T_B^{X,O} \sim 2 \times 10^6$ K) emerges from the lowest layer. This emission is then attenuated in the overlying cooler layer, in which magnetic fields sufficient

for gyroresonance absorption cause the optical depth (and hence the attenuation) to be greater for the X-mode (L) than for the O-mode (R). This results in the emission of O-mode-dominated (R) emission. The polarization is then inverted to its observed (L) value upon traversal of the overlying quasi-transverse (QT) layer in the magnetic field overlying the plage.

Postal Addresses

Jeffrey W. Brosius and Gordon D. Holman
Code 682.1
NASA/Goddard Space Flight Center
Greenbelt, MD 20771

Joan T. Schmelz
Code 602.6
NASA/Goddard Space Flight Center
Greenbelt, MD 20771

Robert F. Willson
Physics and Astronomy Dept.
Tufts University
Medford, MA 02134

Fig- 1

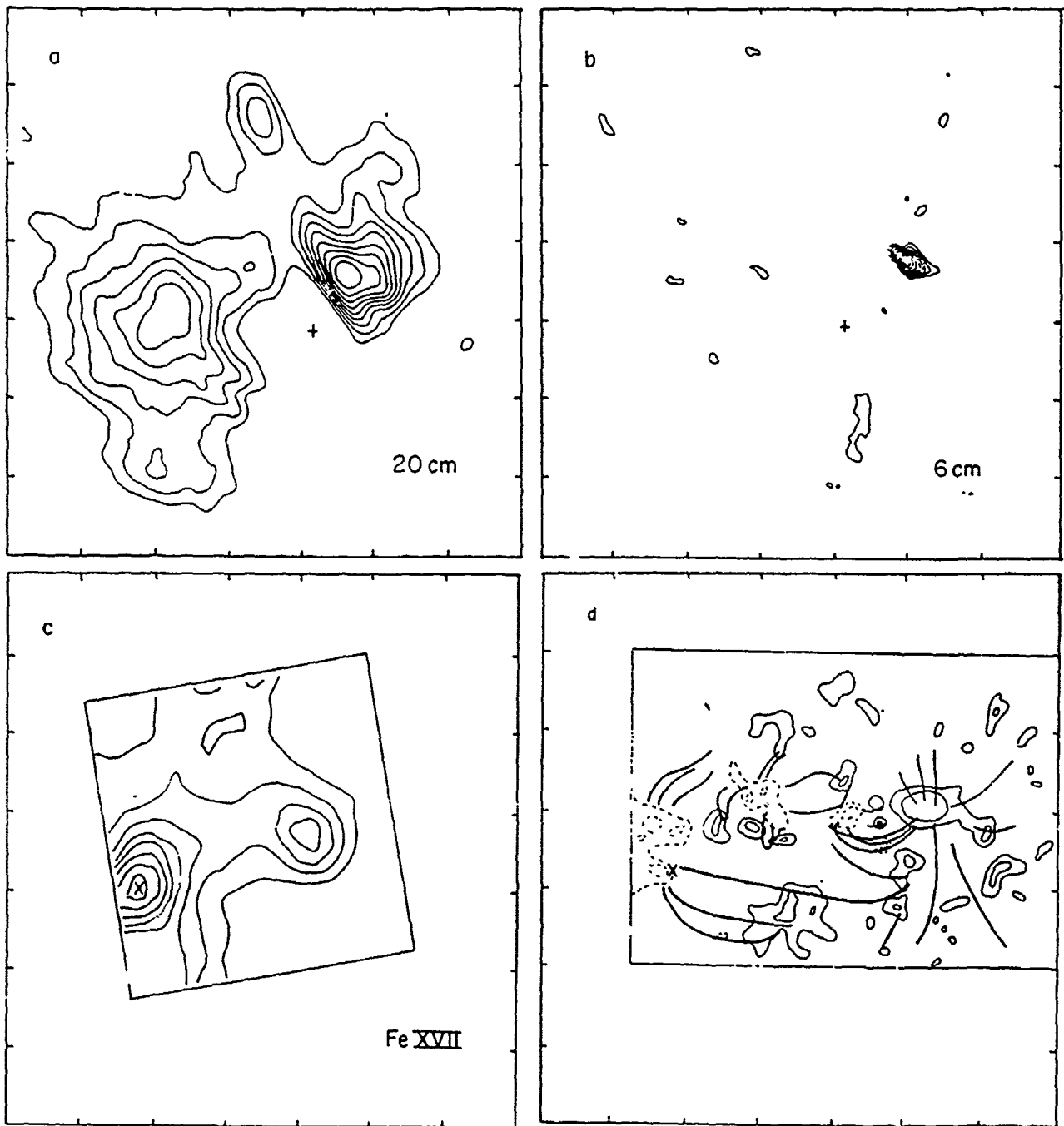


Fig. 1

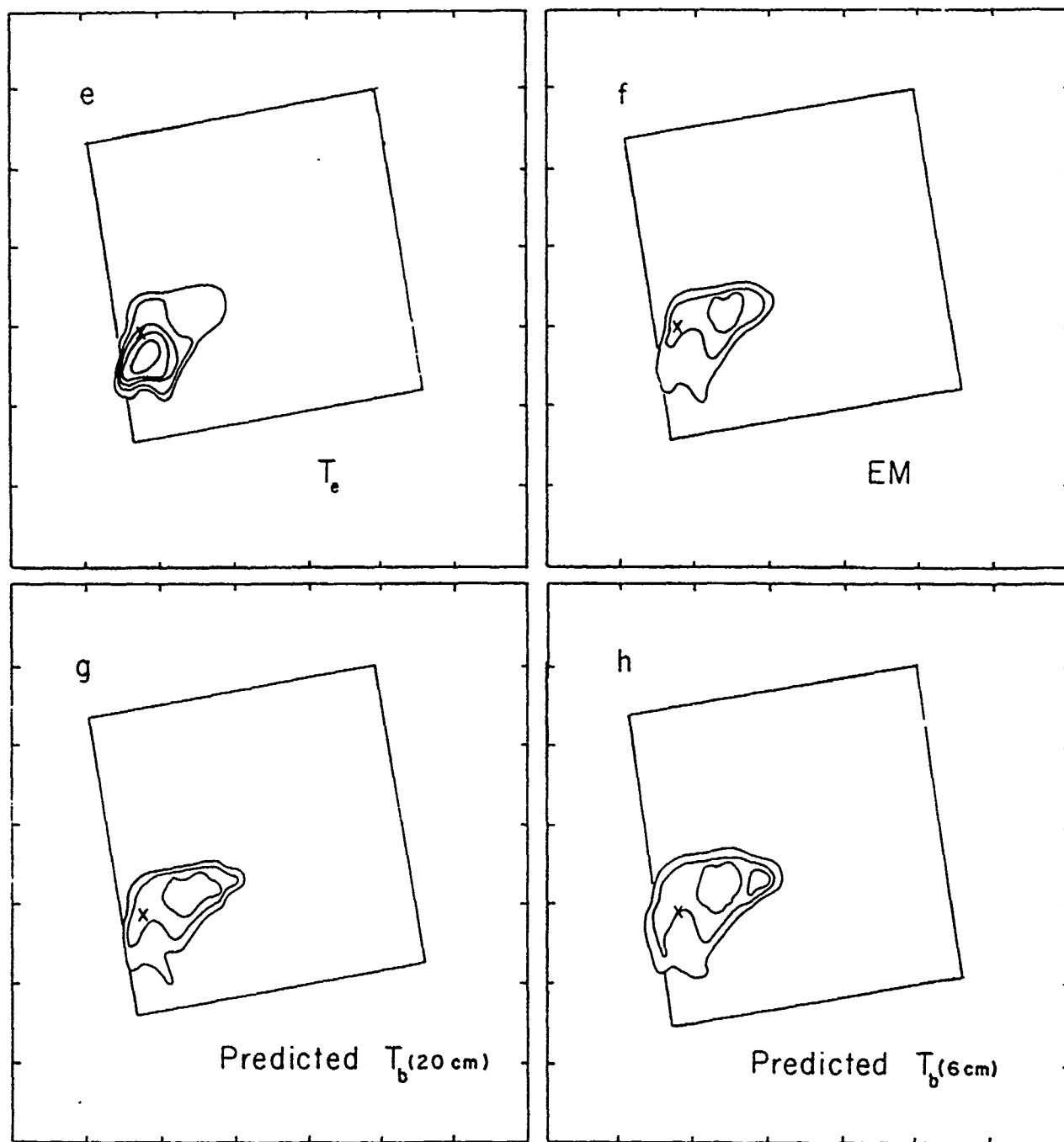


Fig. 2

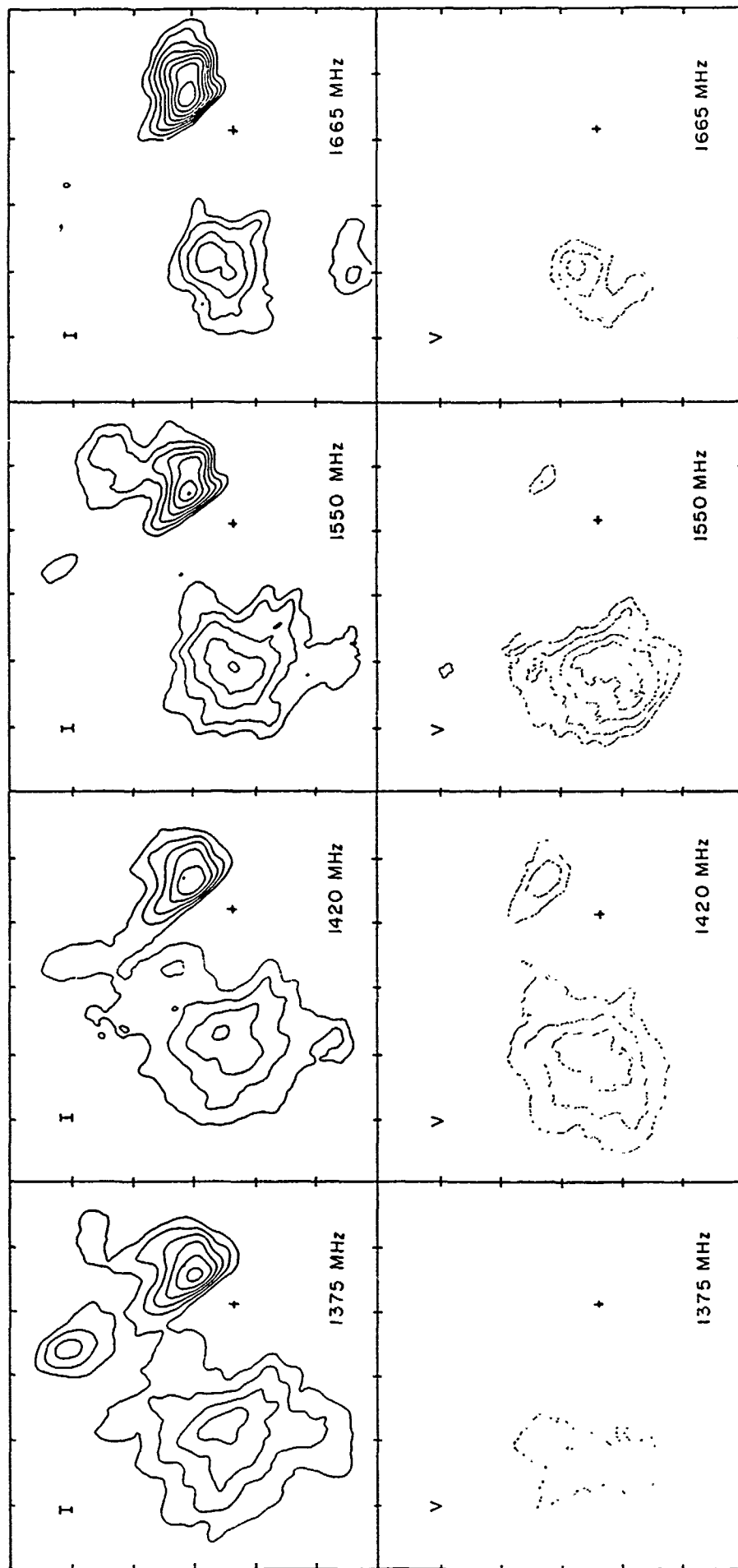


Fig. 3

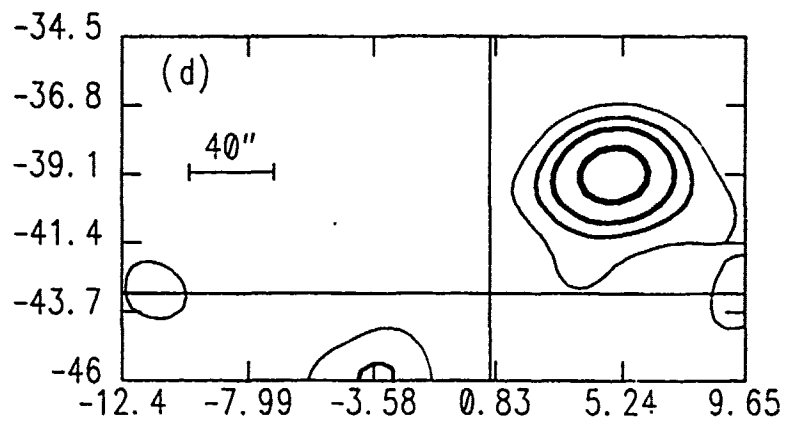
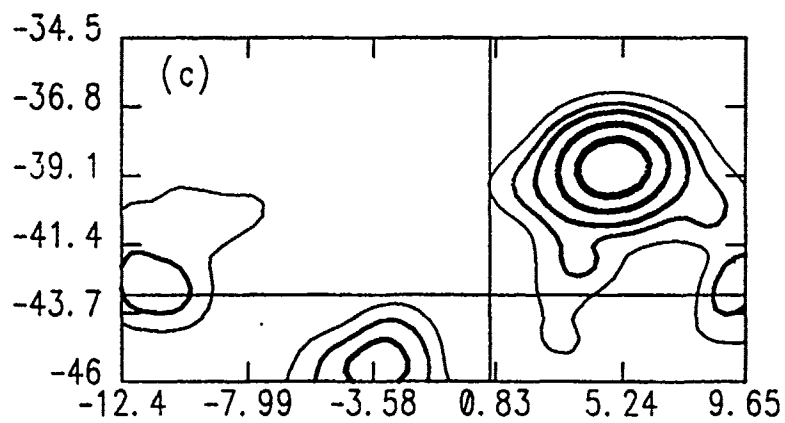
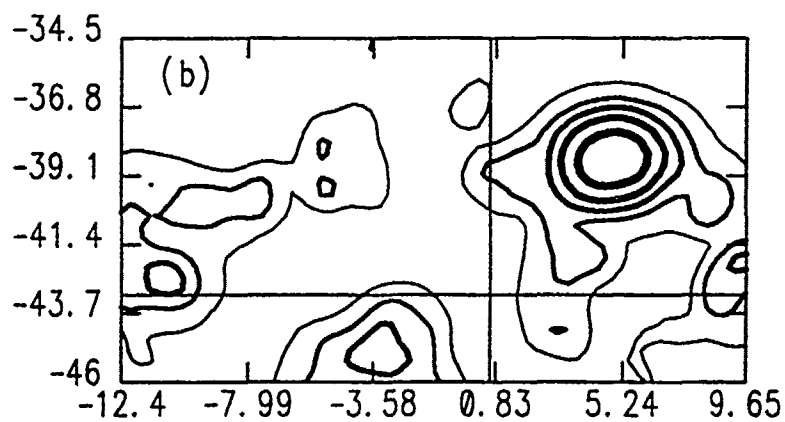
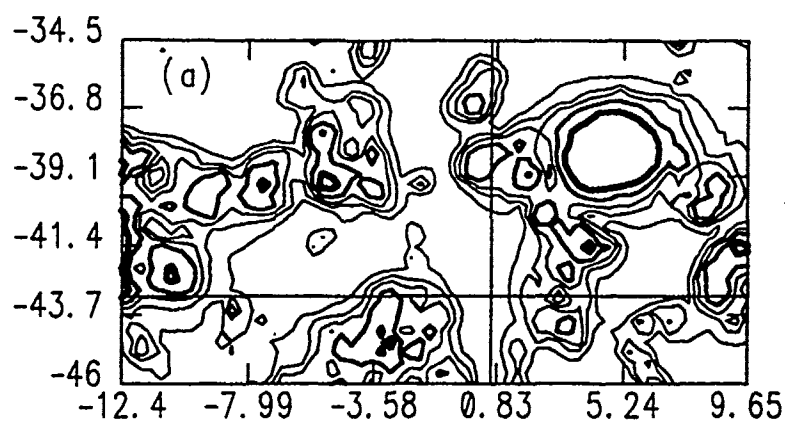


Fig. 4

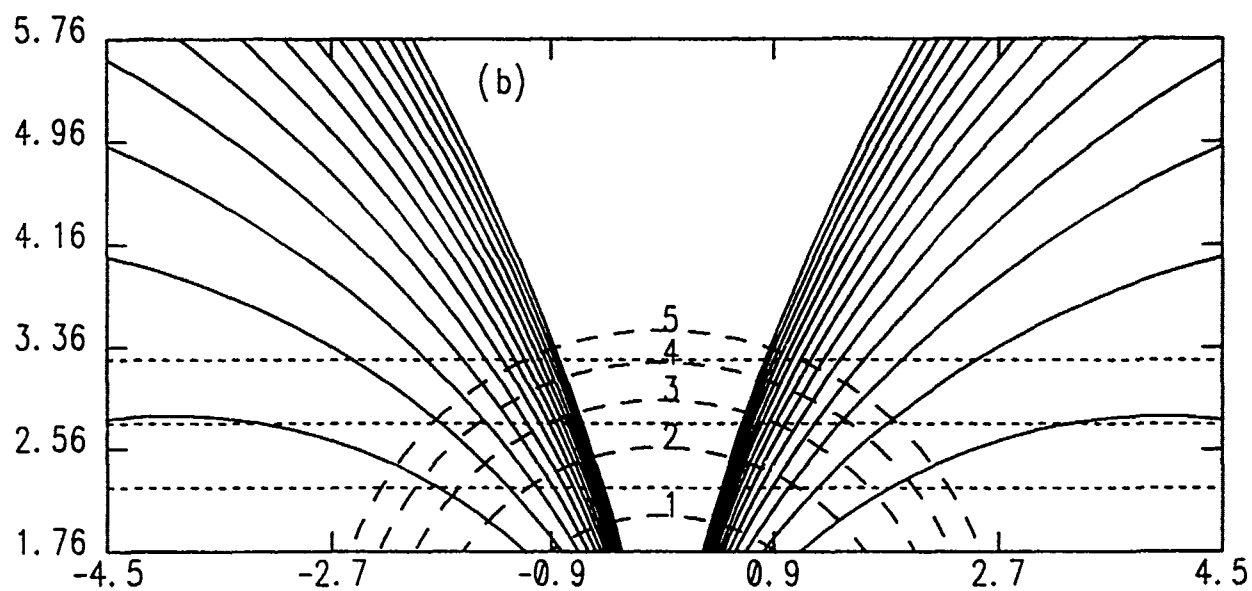
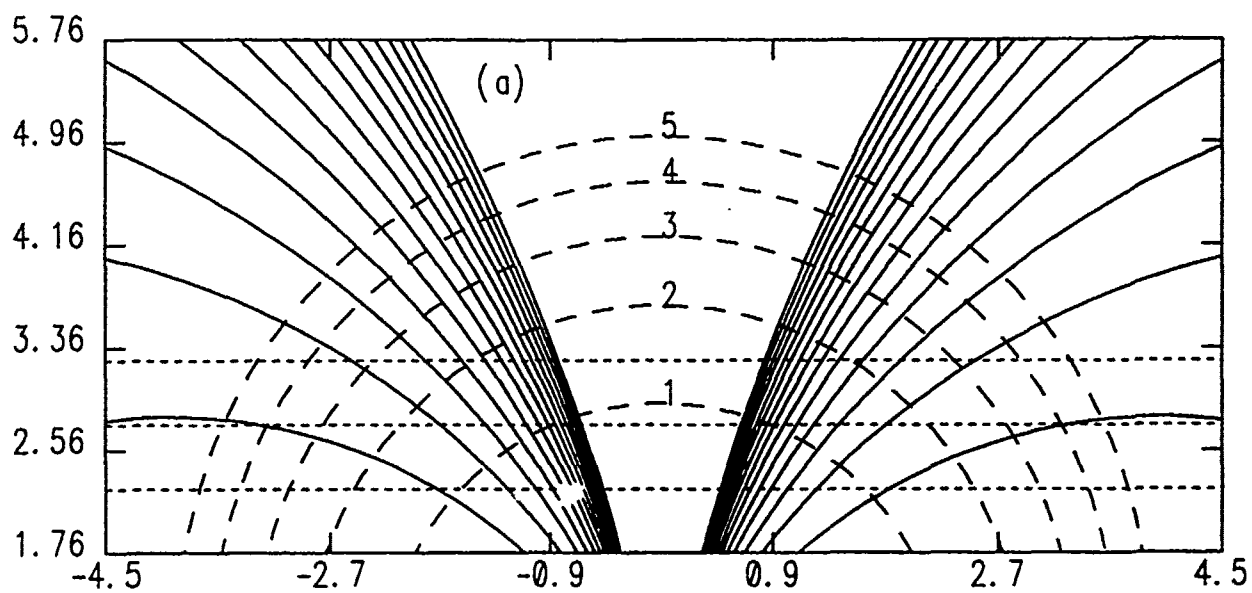


Fig. 5

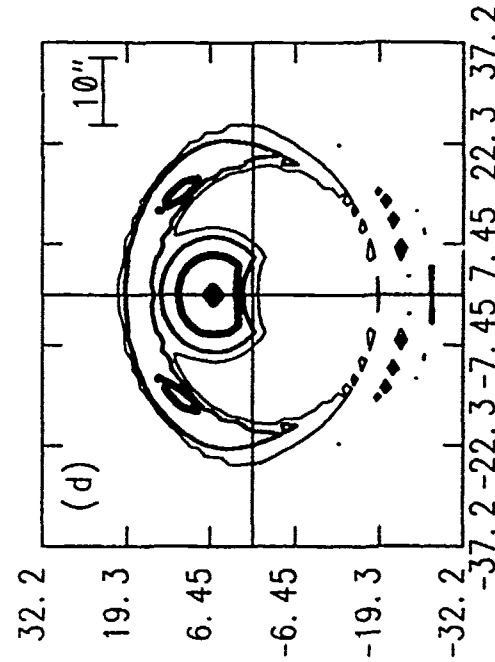
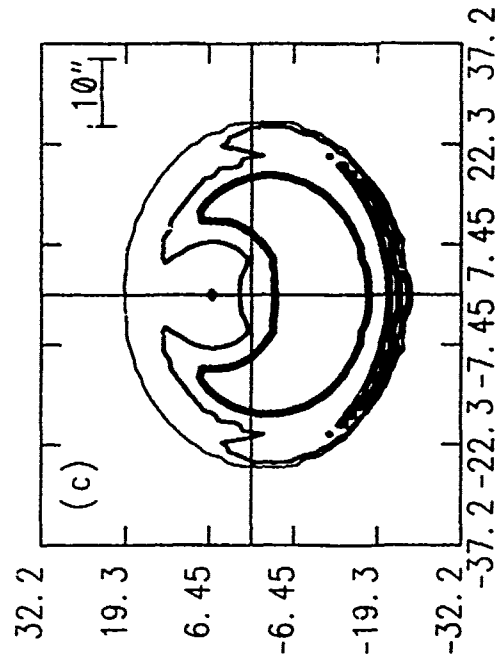
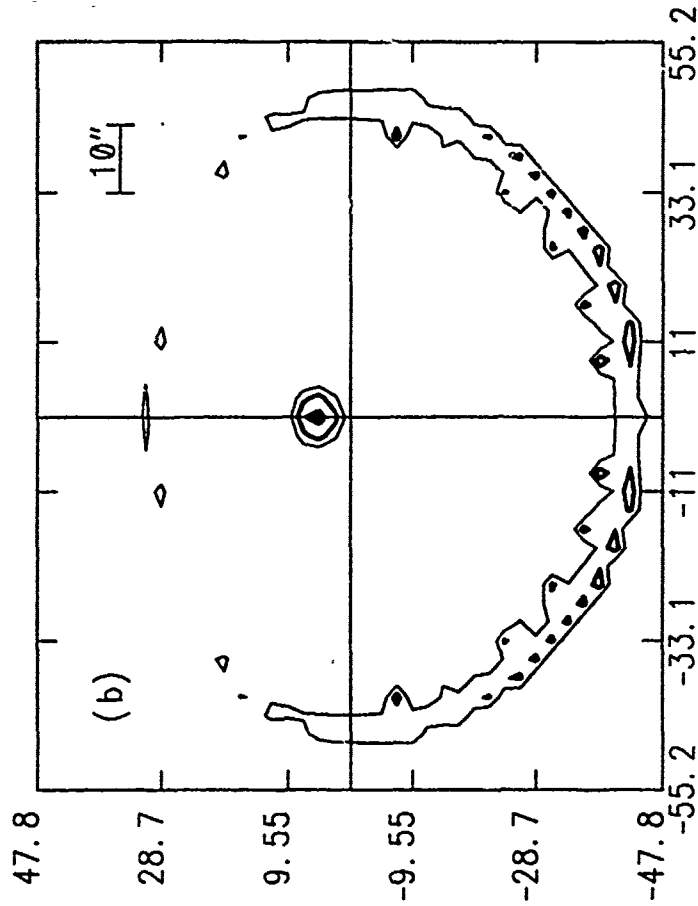
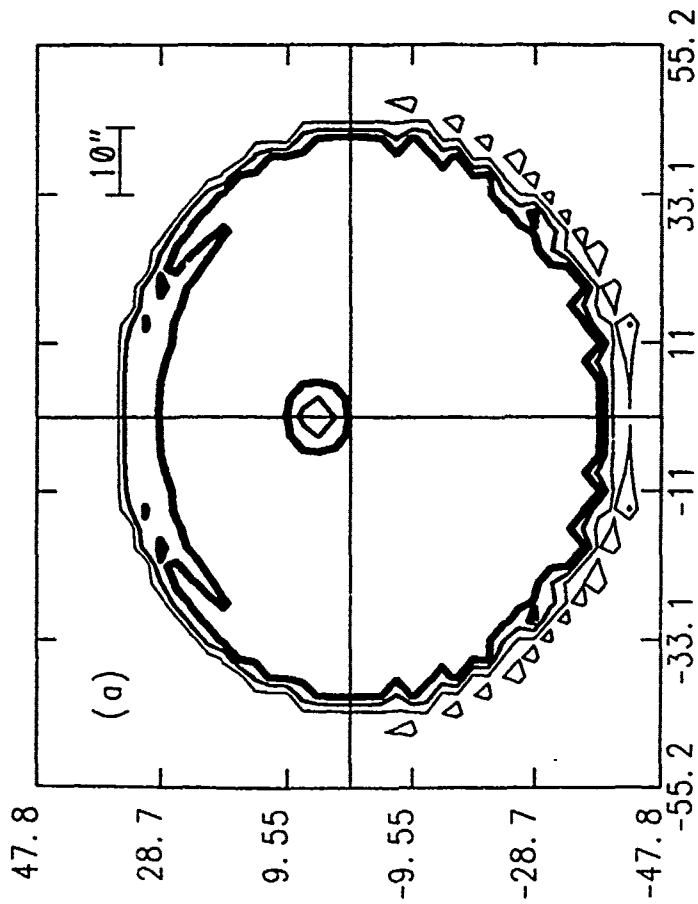


Fig. 6

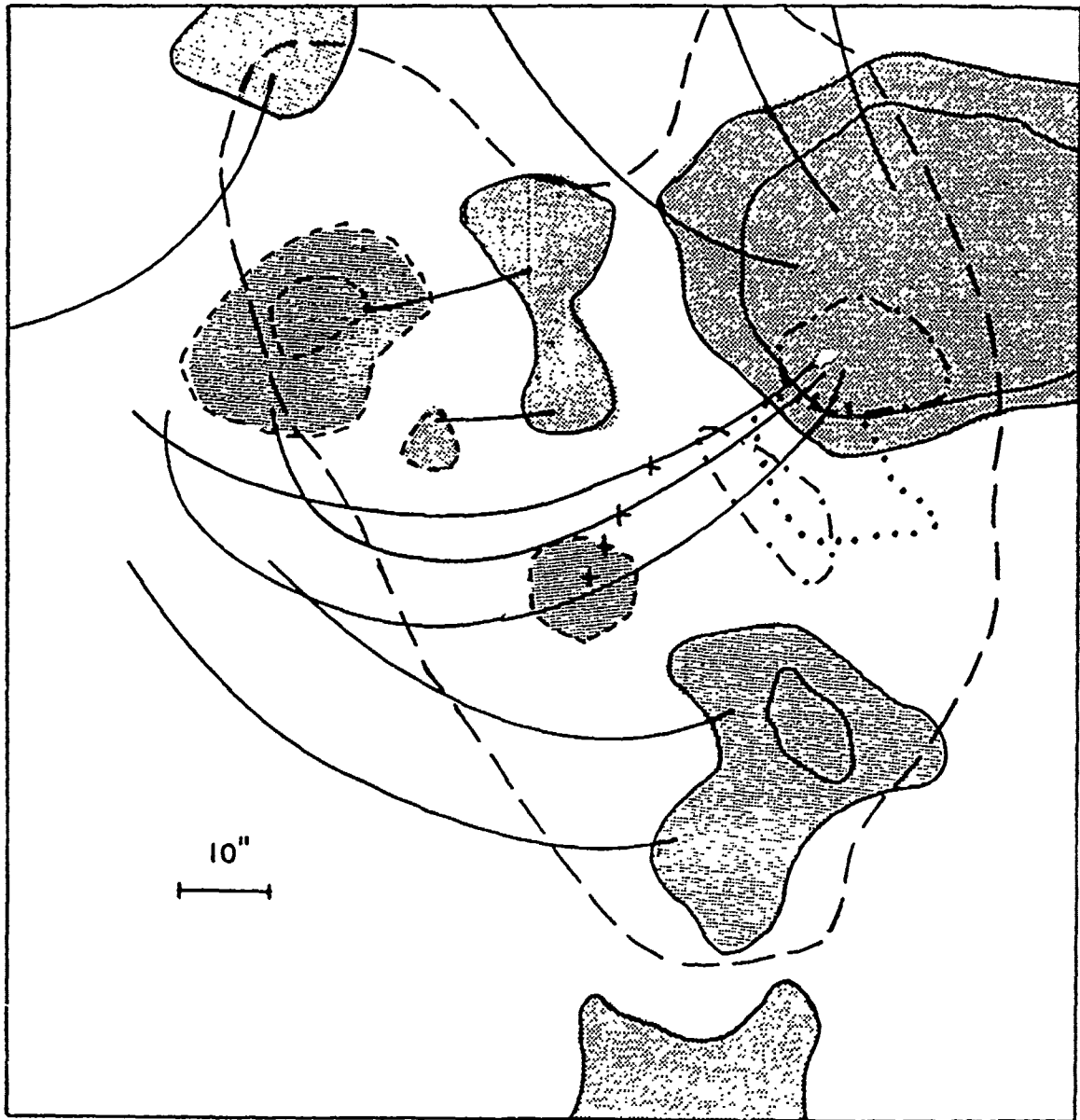


Fig. 7

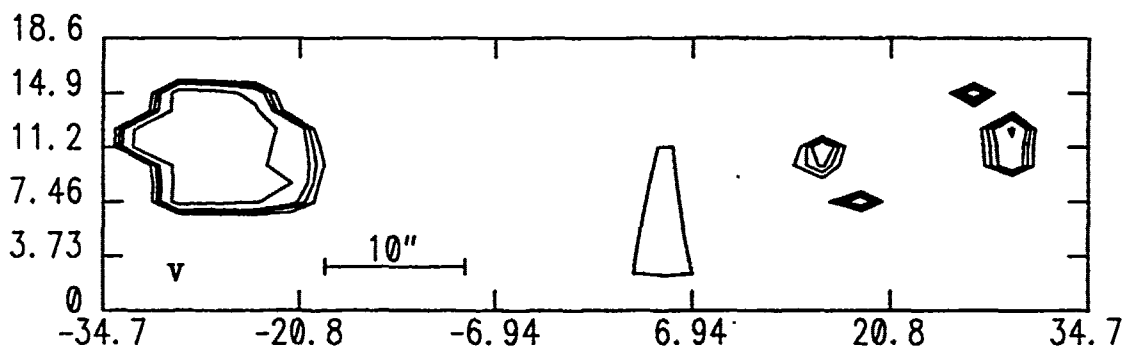
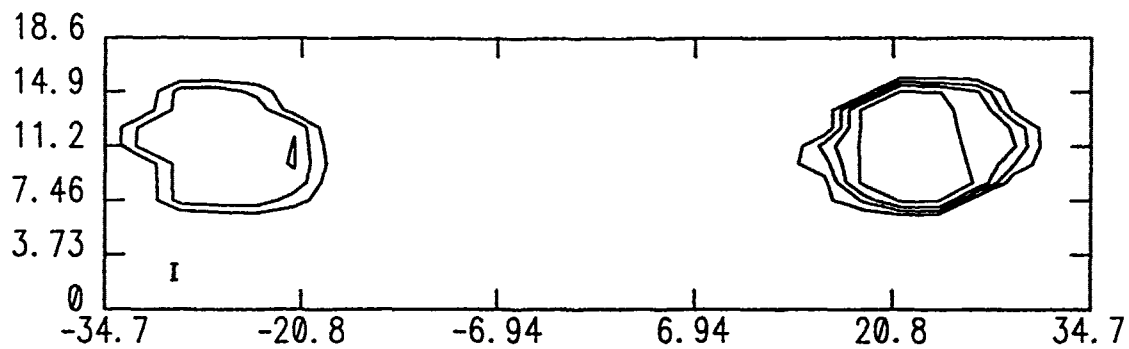


Fig. 8

